Supporting Information

Narasimha et al. 10.1073/pnas.1112281108

SI Materials and Methods

1. Detailed Description of Experimental Setup. A line diagram of the apparatus used in the present work is shown in Fig. S1 (see Fig. 2 in the main text for the photo schematic). It consists of a glass test tank with a cross section of 1 m × 1 m and height of 1.5 m. Tank fluid is nonconducting (mostly deionized water or a solution of organic compound). A plume chamber is attached to a 12 mm thick acrylic sheet (0.98 m square), which serves as a base plate, with the chamber axis aligned to the center-axis of the plate. The base plate also carries an arrangement consisting of four diffuser sectors, one at each corner, to introduce into the tank a urea solution (with specific gravity approximately 0.1% higher than that of the deionized water) for effecting step stratification at z_{ls} (Fig. S1). The active fluid is heated in the plume chamber by an immersion heater (1–2 kW capacity) and is supplied by a constant-head tank on the top of the test tank. Plume heating is controlled by varying input voltage. The heater is surrounded by a copper dome to collect air and steam bubbles, which are released out of the test tank through a vent tube. A brass plug with 4 mm diameter orifice is attached to the top of the plume chamber through which a plume or a jet of active fluid is introduced into the tank. The orifice is mounted on an axisymmetric convergent section, divided into two parts with area ratios of 16 and 121 respectively, that acts as a contraction to improve flow quality. A calibrated flow-control valve is used to vary the flow rate through the orifice. A swivelling mechanism is provided to open or close the orifice as desired.

Another acrylic plate is fixed on the top of the plume chamber (Fig. S1) to provide a well-defined lower boundary condition for studying flow entrainment characteristics (1). An off-source heater, consisting of six wire-mesh electrodes supported on a nylon frame, is placed on this dividing plate. The meshes are made of SS316 grade steel wires of 100 μm diameter. The Reynolds number based on wire diameter and typical velocity in the heat injection zone (HIZ) is less than 10; the electrodes therefore have negligible influence on the flow (2).

The individual electrodes are connected to a high frequency (approximately 16 kHz) square-wave power supply through a control panel which allows any electrode to be connected to or disconnected from the circuit. Input voltage can be varied over the range 0–250 V using a variable transformer (Variac). The high frequency supply helps avoid electrolysis of the active fluid at the electrodes (3). Incidentally, though the frequency is high, the heater has negligible inductive losses and so is primarily resistive.

Another heater (nichrome wires stretched zig-zag across an acrylic frame) is immersed below the free water surface at the top, and serves two purposes. Firstly it avoids possible adverse influence on the flow due to jet/plume oscillations (2), and secondly it simulates (when required) an inversion layer of the kind often present in the atmosphere at higher altitudes (z_{us}). Three resistance temperature detectors (RTDs) are used to measure temperature; two of them are in the plume chamber and the third is mounted in the plane of the free-surface heater. The third RTD is also used to measure the ambient temperature in the tank. A data logger (Agilent 34972A), which acquires voltage, current and temperature signals, is connected to a computer providing real-time monitoring of all signals. A Nikon D-90 DSLR camera is used to record videos.

2. Comparison Pictures with Details. See Fig. S2.

3. Calculation of Entrainment-Coefficient Values. The variation of the Taylor entrainment coefficient α_E in the vertical, shown in Fig. 4 in the main text, has been obtained by reanalysis of five datasets (four on steady jets and one on steady plume) published in the literature. They have been measured in three different laboratories namely Indian Institute of Science (IISc), Delaware University (DU), and Florida State University (FSU), all using a setup very similar to that developed by Bhat and Narasimha (2).

Calculation of α_E requires accurate measurements of mass-flow rate and velocity width. In the present apparatus useful run time is limited to 15–20 min, as properties of the ambient fluid slowly change during the run. This constrains data-averaging time. As a result estimates of α_E in experiments show some scatter and sometimes exhibit rather large fluctuations, amplified further by the need to evaluate z-derivatives of the mass-flow-rate values. There are certain other sources of uncertainty also, such as (*i*) the difficulties encountered in measuring small velocities close to jet/plume edges, and (*ii*) the presence of heating grids in the measurement zone causing unwanted reflections. Thus, to get reasonable estimates of α_E, some data smoothing is necessary. In the following, we present a brief account of the procedure used to arrive at the α_E values for each dataset.

1. Bhat and Narasimha (2) (BN-IISc): Bhat and Narasimha used laser Doppler velocimetry (LDV) to measure the velocity field for a jet with off-source heating. For smoothing the trend, the mean centerline velocity (U_c) was corrected at two streamwise locations; one close to and the other upstream of the beginning of the HIZ (z_b). For this the expression for U_c for the unheated jet given in table 1 in ref. 2 was used. Bhat and Narasimha have reported velocity widths (b_{ue}, where $U(b_{ue}) = U_c/e$) for some heights inside and beyond the HIZ. The values of b_{ue} upstream of z_b were obtained from the measured scalar widths b_{se}, using the standard ratio $b_{se}/b_{ue} = 1.3$ reported in ref. 2 for the unheated jet. This ratio varies with heat injection and has therefore not been used for $z > z_b$. Since the measured axial velocity profiles are approximately Gaussian, mass-flow rate was obtained as $m = \rho\pi b_{ue}^2 U_c$.
2. Agarwal and Prasad (4) (AP-DU): Agarwal and Prasad performed particle image velocimetry (PIV) measurements on a jet with off-source heating, both outside and inside the HIZ. They observed large scatter in their data (U_c, b_{ue} and m), and attributed it to the presence of heating grids in the HIZ and not to insufficient averaging time. To assess the trend of the data, we have drawn faired curves through the data points and used these curves for calculating α_E. As the scatter in m is quite large, two relatively extreme choices for the faired curve were identified; the width of the band in Fig. 4 in the main text reflects this spread. Furthermore, there appears to be a mistake in the line drawn in the velocity-width plot (figure 9 in ref. 4) for the unheated jet. From the slope of the line it appears that Agarwal and Prasad compare b_{ue} for the heated jet with b_u (defined by $U(b_u) = U_c/2$) for the unheated jet. This could result in errors in calculating α_E/α_{Eb}, since α_{Eb} (i.e., α_E at z_b) obtained from heated jet data should match with the value for the unheated jet. To make sure that our estimates of α_E/α_{Eb} for this dataset are reasonably accurate, we have calculated α_E for the unheated jet using the corrected value of the slope (0.11 instead of 0.09) in figure 9 in ref. 4. The two faired curves through the data on m, in the heated jet, are then fitted so that as $z \to z_b$, α_E approaches the value for the unheated jet consistent with the corrected slope.

3. Venkatakrishnan (5) (V_T-IISc): Venkatakrishnan studied both jets and plumes using LDV. We have used two datasets from his experiments; one for a jet and the other for a plume. The variation of mass-flow rate (figures 3.19 and 4.20 in ref. 5) shows some sharp changes (possibly due to measurement uncertainties), so we have used a smooth curve drawn within the error bars to evaluate dm/dz. Note that Venkatakrishnan reports "half-velocity" width (b_u) rather than b_{ue}. However, this does not matter in the final analysis since we plot only the ratio α_E/α_{Eb} (i.e., the relative change in α_E over its value at z_b) which takes care of the differences in the definition of b.
4. Venkatakrishnan et al. (6) (VK - FSU): Venkatakrishnan et al. report PIV measurements on jets with off-source heating, and provide velocity-field data only downstream of HIZ for heated and unheated jets. The α_E was calculated based on direct measurement of radially-inward velocity at b_{ue}. Venkatakrishnan et al. observed large spatial fluctuations (associated presumably with the passing of coherent structures) in their α_E plot for both unheated and heated jets (figure 7 in ref. 6). However, mean lines through their data are well defined because of the large spatial extent covered in the experiments, and we have used such mean values of α_E for the present purposes.

All the datasets mentioned above [two from Venkatakrishnan (5), one each from the rest] have been displayed in Fig. 4 in the main text. The width of the band for each dataset indicates the spread or variability due to choice of faired curves or to obtaining smoothed trends. Note that the dataset in ref. 7 has not been included here since the experimental conditions therein were broadly similar to those in Venkatakrishnan (5), which is preferred because it reports more experiments suitable for the present analysis.

All the G values in Fig. 4 in the main text have been calculated using b_{ue}. For this purpose, the value of b_{ue} in the datasets of Venkatakrishnan (5) was estimated by multiplying b_u by 1.2 (which is valid since the measured velocity profiles were approximately Gaussian).

The summary plot (Fig. 4 in the main text) shows remarkable agreement between the datasets of Bhat and Narasimha (2) and Venkatakrishnan (5) (involving calculation of α_E using velocity profiles measured by LDV) and that of Venkatakrishnan et al. (6) (involving direct measurements of entraining velocities using PIV) for $(z-z_b)/l > 1.4$. This confirms the overall consistency of the present analysis. The fifth dataset due to Agarwal and Prasad (4) stands out and shows much larger variations even though the value of G is of the same order. The α_E values for an extreme choice of the faired curve for the Agarwal and Prasad data become negative, implying detrainment, which is not observed in any of the other studies. Moreover, beyond the HIZ, α_E rises to large positive values much higher than those of Venkatakrishnan et al. (6) and others. Possible reasons for these differences are the following: (*a*) Turbulence levels at the bottom of the HIZ are unusually high in Agarwal and Prasad (4) [$u'/U_c \cong 0.4$ as against 0.25 for Bhat and Narasimha (2); the latter is close to that for classical jets (8)]. These are likely due to higher concentration of acid (15 mL/L of water) used by Agarwal and Prasad (4) as compared to Bhat and Narasimha (2) (2 mL/L). (*b*) Agarwal and Prasad (4) note that their measured velocity profiles inside the HIZ are flat-top Gaussian and the mass-flow rate (figure 14 in ref. 4) calculated based on the Gaussian assumption (which they used for calculating m) is likely to be an underestimate. It is possible that this is responsible for the dip in the variation of m seen in figure 14 in ref. 4. (*c*) There are difficulties in measuring velocity inside the HIZ in the presence of heating grids [as recognized by Agarwal and Prasad (4)]. (*d*) The height of HIZ in Agarwal and Prasad (4) is relatively short. Table S1 presents the ratio of the HIZ height to the flow width at the beginning of the HIZ ($L/b(z_b)$) (along with other relevant length ratios) for the datasets under consideration. It is seen that Agarwal and Prasad (4) had $L/b(z_b)$ of only 2.36, compared to the values 4.5–7.33 in the other four experiments. This would imply fewer coherent structures in the HIZ in the experiments of Agarwal and Prasad (4), with correspondingly longer time scales and hence also averaging times required to get sufficiently precise statistics on the quantities of interest.

4. Flow Visualization Images of Steady Diabatic Plumes. In the main text, we have mentioned the effect of off-source heat addition on the large-scale turbulence structure of steady jets and plumes, namely presence of protected cores, disruption of coherent structures etc. Here we present laser-induced fluorescence pictures from some of the previous studies on steady plumes, as evidence of these effects.

Fig. S3 shows a comparison of time-averaged dye concentration in vertical sections of unheated and heated plumes (7, 9). It is evident from the figure that the dye concentration in the core of the heated plume is much higher than that in the unheated counterpart, implying reduction in entrainment upon heat addition in the upper region of HIZ. Furthermore, the mixing between the plume and ambient fluid inside the HIZ is limited to an annular region ("ring") surrounding the core which remains largely protected.

Horizontal cross-sections of the instantaneous flow pictures for unheated and heated plumes are shown in Fig. S4. The presence of the protected core along with a surrounding ring are again clearly seen, as also the disruption of the large-scale structures.

5. Calculation of Diabatic Purity for Laboratory Flows. In *Materials and Methods* in the main text, we used $(d/dz)\int_A(c\dot{m})dA \cong 0$. Here we provide the reasoning behind it. For convenience, throughout this section, we denote time-averaged quantities with an overbar, so the above equation becomes $(d/dz)\int_A(\bar{c}\,\bar{\dot{m}})dA \cong 0$. The time-averaged total flux of concentration is given by $F(z) = \int_A(\overline{c\dot{m}})dA = \int_A(\bar{c}\,\bar{\dot{m}} + \overline{c'\dot{m}'})dA$, where primes indicate fluctuating turbulent quantities. For thin shear layers (like the steady diabatic flows considered here), the turbulent transport of dye concentration ($\overline{c'\dot{m}'}$) is expected to be only a small fraction of the mean transport ($\bar{c}\,\bar{\dot{m}}$). Also in the integral formulation of thin jets and plumes (10), which is directly applicable here, $(\partial/\partial z)(\overline{c'\dot{m}'})$ is neglected in comparison with $(\partial/\partial z)(\bar{c}\,\bar{\dot{m}})$. This implies $F(z) \cong \int_A(\bar{c}\,\dot{m})dA$, and because there are no sources or sinks of dye particles in the experiments $F(z)$ is invariant in z; i.e., $(d/dz)\int_A(\bar{c}\,\bar{\dot{m}})dA \cong 0$.

Some additional remarks on the purity comparison in Fig. 5 in the main text.

1. The diabatic purity for the laboratory flows has been calculated by using the smoothed mass-flow-rate data obtained by the methodology outlined in section 3 above.
2. In the main text we have shown that $\bar{p}_d(z) = [1 + \int_{z_b}^{z}(2\pi\rho\alpha_E\bar{b}\bar{U}_c)dz/\bar{m}(z_b)]^{-1}$. Thus the shape of the average diabatic-purity curve is directly linked to the variation in the entrainment coefficient α_E (Fig. 4 in the main text). As a result, the favorable comparison of purity between laboratory experiments and cloud-resolving model (CRM) computations can be seen as a consequence of the realistic variation of α_E captured in the experiments.
3. As noted in the main text, the height $z - z_b = 1.8$ km is used for normalizing heights from the CRM computations. Independent but indirect support for this choice comes from the vertical variation of buoyancy given in figure 8 in Romps and Kuang (11). There is a local peak around $z - z_b = 1.4$ km (followed by another peak at a higher altitude), which is close

to the value of 1.8 km used above. Even though the buoyancy consists of contributions from both specific heat and latent heat, it gives a rough indication of the altitude (1.4–1.8 km above the cloud base) by which most of the latent heat of condensation has been released. This lends further support to the choice of $z - z_b = 1.8$ km as the appropriate length scale.

Protected cores in deep convective clouds. Romps and Kuang (11) have shown that the flux of undiluted plumes above 4–5 km is negligible, and that it is therefore unlikely that undiluted parcels from cloud base can reach high altitudes close to the tropopause. This appears to cast doubt on the validity of the protected-core idea proposed by Riehl and Malkus (12) for deep clouds. On the other hand, our laboratory experiments clearly show the presence of protected cores as a consequence of the disruption of coherent structures due to diabatic heating (see Figs. S3 and S4). These observations are not as contradictory as they seem. To see this, note that the effect of off-source diabatic heating is to first enhance the entrainment rate and hence cause large dilution, and then to suppress it further above causing much lower dilution. The protected cores are likely to emerge only in the regions of low dilution rates associated with coherent-structure disruption. Thus it is unlikely that the protected cores would be present right from the cloud base to high altitudes in deep clouds, but only in certain altitude ranges dictated by the dynamical effects of the latent-heat release. For example, from figure 3 in ref. 11, it is possible to infer the presence of protected cores in two height ranges (above z_b): 1.5–2.5 and 5.5–7.5 km, wherein the purity variation, especially in cloud cores, is much weaker. But because the entrainment rates are large at other heights causing significant dilution, these protected cores are likely to contain diluted parcels and not only those that originate at the cloud base. This is consistent with the results of ref. 11.

6. Homogeneous/Inhomogeneous Mixing in Cumulus Clouds. The distinction between homogeneous and inhomogeneous mixing in clouds is based on the value of a nondimensional group called Damkohler number given by

$$Da = \frac{\tau_{\text{mix}}}{\tau_{\text{react}}},$$

where τ_{mix} is the turbulent mixing time scale and τ_{react} is the "reaction" time scale associated with the phase change; i.e., droplet evaporation in the present context. τ_{react} is shown to depend on the rate of droplet evaporation and that of phase relaxation (13). The mixing time scale is given by $\tau_{\text{mix}} = (l_E^2/\epsilon)^{1/3}$, where l_E is the length scale of an entrained parcel, and ϵ is the turbulent kinetic energy dissipation rate. If $Da < 1 (> 1)$, the mixing is said to be homogeneous (inhomogeneous).

Gerber et al. (14) have carried out airborne measurements of trade-wind cumulus clouds at different altitudes. Here our aim is to calculate the variation of τ_{mix} with height in the clouds measured by them. For this purpose we choose two altitudes: level 1 (252 m above cloud base) and level 4 (918 m above cloud base). The measured values of mean ϵ are 14.01 cm^2/s^3 at level 1 and 74.61 cm^2/s^3 at level 4 (14). Gerber et al. (14) have reported size distribution of all of the entrained-parcel lengths (l_E) from level 1 to 4, but not their variation with height. Raga et al. (15), in their cloud measurements, find that the maximum value of the length scale of the entrained parcels (l_E) increases rapidly above the cloud base, and then shows a mild decrease further above. Drawing cues from this observation, we may take the value of l_E in the measured clouds in (14) to be constant with height at 1.6 m, the measured geometric mean value (14). Using these numbers, we obtain the following values for the mixing time scale: $\tau_{\text{mix}} \approx 12$ s at level 1 and $\tau_{\text{mix}} \approx 7$ s at level 4. Note that if l_E decreases with height (as in ref. 15), the difference in τ_{mix} between levels 1 and 4 will become even more pronounced.

Next we estimate τ_{mix} in the laboratory experiments of Bhat and Narasimha (2). The expression for dissipation is given by $\epsilon(z) = a(z)u^3/l$, where u and l respectively are the velocity and length scales of typical large eddies, and a is a constant of proportionality. Because the variation of a with height is not available in the measurements, it is not possible to calculate ϵ directly. However, following Baker et al. (16) it is reasonable to assume that at a given z the proportionality constant would remain the same for a range of eddy sizes across the inertial subrange. We can therefore write $\epsilon(z) = au^3/l = au_E^3/l_E = al_E^2/\tau_{\text{mix}}^3$, which gives $\tau_{\text{mix}} = (l_E^2 l/u^3)^{(1/3)}$. Table S2 shows values of different quantities at two heights in the experiments of (2)—one at the base of the HIZ and the second just above the end of the HIZ.

The large-eddy velocity scale (u) at both heights is taken to be the maximum rms value of the measured axial velocity fluctuations. The choices for l and l_E need some consideration. For this we are guided by the instantaneous flow visualization pictures of the planar sections of these flows reported in refs. 2 and 9 (see also Fig. S4). By close examination of these pictures we choose the following values for the length scales. At $(z - z_b)/L = 0$, $l = b$ and $l_E = b/2$; at $(z - z_b)/L = 1.15$, $l = b/2$ and $l_E = b/10$, where b is the velocity width. These choices are supported by the wavelet analysis of the diametral sections of the flow (17) and direct numerical simulations of a temporally growing jet with off-source heating (see figure 10 *a* and *b* in ref. 18). With these estimates, the calculated value of τ_{mix} in the laboratory experiments decreases from approximately 1.5 s at the base of the HIZ to 0.7 s above the HIZ. (Note that different choices for l and l_E do not alter the qualitative picture). Although these numbers are only crude estimates, the overall behavior is not inconsistent with the decrease in τ_{mix} with height observed in natural clouds, nor with the homogeneous mixing scenario.

1. Schneider W (1981) Flow induced by jets and plumes. *J Fluid Mech* 108:55–65.
2. Bhat GS, Narasimha R (1996) A volumetrically heated jet: Large-eddy structure and entrainment characteristics. *J Fluid Mech* 325:303–330.
3. Bhat GS, Narasimha R, Arakeri VH (1989) A new method of producing local enhancement of buoyancy in liquid flows. *Exp Fluids* 7:99–102.
4. Agarwal A, Prasad AK (2004) Evolution of a turbulent jet subjected to volumetric heating. *J Fluid Mech* 511:95–123.
5. Venkatakrishnan L (1997) Development of a plume with off-source volumetric heating. PhD thesis (Indian Institute of Science, Bangalore).
6. Venkatakrishnan L, Elavarasan R, Bhat GS, Krothapalli A, Lourenco L (2003) Particle image velocimetry study of a cloud-like flow. *Curr Sci* 85:778–785.
7. Venkatakrishnan L, Bhat GS, Narasimha R (1999) Experiments on a plume with off-source heating: Implications for cloud fluid dynamics. *J Geophys Res* 104:14271–14281.
8. Narasimha R, Bhat GS (2008) Recent experimental and computational studies related to the fluid dynamics of clouds. *Computational Physics and New Perspectives in Turbulence* ed Kaneda Y (Springer, New York) pp 313–320.
9. Venkatakrishnan L, Bhat GS, Prabhu A, Narasimha R (1998) Visualization studies of cloud-like flows. *Curr Sci* 74:597–606.
10. Turner JS (1973) *Bouyancy Effects in Fluids.* (Cambridge University Press, London).
11. Romps DM, Kuang Z (2010) Do undiluted convective plumes exist in the upper tropical troposhrere? *J Atmos Sci* 67:468–484.
12. Riehl H, Malkus J (1958) On the heat balance in the equatorial trough zone. *Geophysica* 6:503–538.
13. Lehmann K, Siebert H, Shaw RA (2009) Homogeneous and inhomogeneous mixing in cumulus clouds: Dependence on local turbulence structure. *J Atmos Sci* 66:3641–3659.
14. Gerber HE, Frick GM, Jensen JB, Hudson JG (2008) Entrainment, mixing and microphysics in trade-wind cumulus. *J Meteorol Soc Jpn* 86A:87–106.
15. Raga GB, Jensen JB, Baker MB (1990) Characteristics of cumulus band clouds off the coast of Hawaii. *J Atmos Sci* 47:338–355.
16. Baker MB, Breidenthal RE, Choularton TW, Latham J (1984) The effects of turbulent mixing in clouds. *J Atmos Sci* 41:299–304.

17. Narasimha R, Saxena V, Kailas SV (2002) Coherent structures in plumes with and without off-source heating using wavelet analysis of flow imagery. *Exp Fluids* 33:196–201.

18. Basu AJ, Narasimha R (1999) Direct numerical simulation of turbulent flows with cloud-like off-source heating. *J Fluid Mech* 385:199–228.

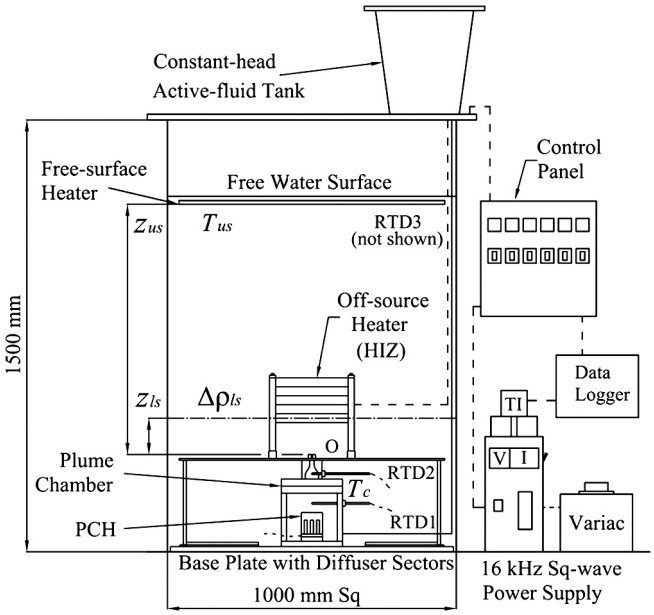

Fig. S1. Schematic of the present experimental setup. O: orifice (with diameter $d = 4$ mm), TI: temperature indicator. V and I: voltmeter and ammeter respectively. PCH: plume chamber heater. Dashed lines are electrical wires. RTD: resistance temperature detector. For other symbols see Fig. 2 caption in the main text.

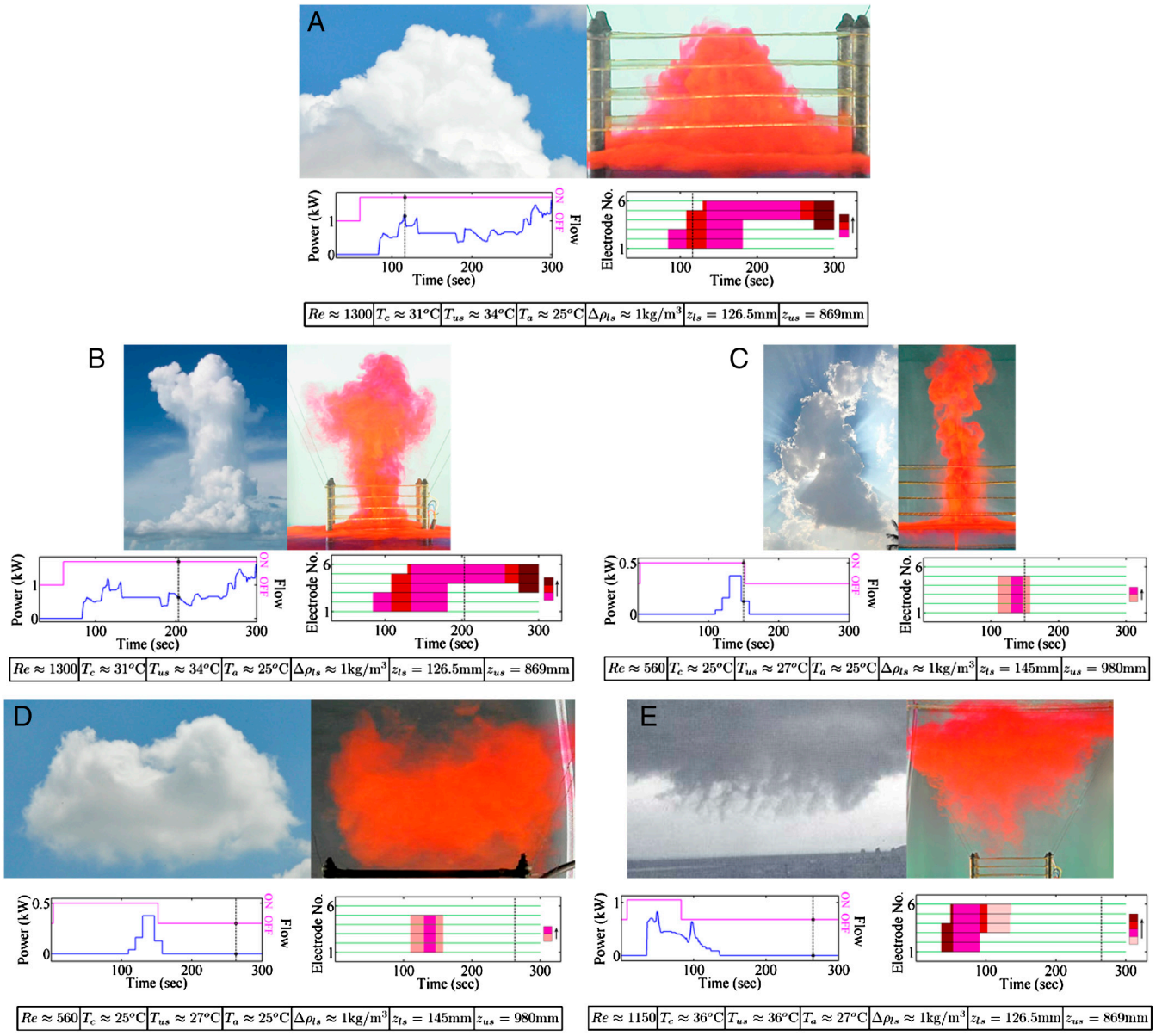

Fig. S2. (*A–E*) Heating histories, profiles, and other details for the simulated clouds shown in Fig. 3 in the main text. The comparison pictures are reproduced here for the sake of completeness. Backgrounds of some of the images are selectively blurred using a Gaussian filter. Note that the color code used in the lower-right panel for each comparison (showing heating profile) is qualitative and has been added for better representation of the actual region in the HIZ in which heat is being added. The same applies to Fig. 3 in the main text as well.

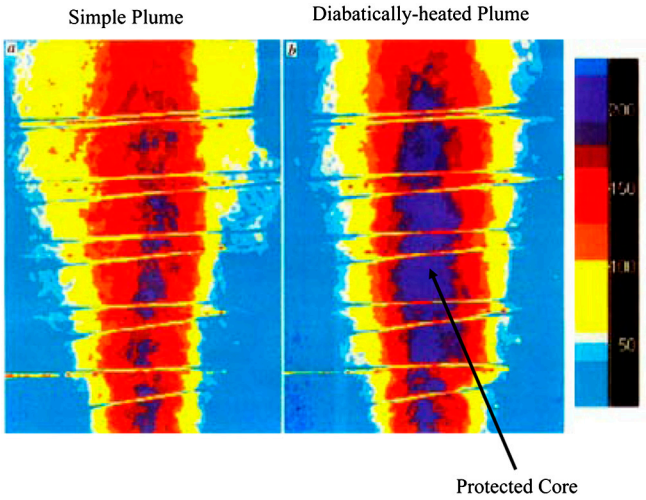

Fig. S3. Time-averaged pictures of vertical sections (inside the HIZ) of the (*Left*) unheated plume showing progressive dilution by entrainment and (*Right*) heated plume ($Q = 555$ W) showing nearly protected core. Reprinted with permission from Current Science Association (9).

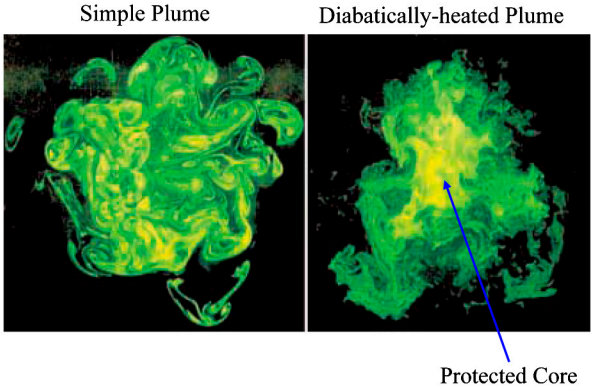

Fig. S4. Instantaneous laser-induced fluorescence images of horizontal (diametrical) sections of plume inside the HIZ. (*Left*) Unheated, (*Right*) heated ($Q = 555$ W). Protected core in the heated flow can be clearly seen. Reprinted with permission from Springer Science + Business Media (figure 2 in ref. 17).

Table S1. Certain geometric parameters in the laboratory experiments on steady diabatic jets and plumes

Dataset	z_b/d	L/d	$b(z_b)/d$	$L/b(z_b)$
BN	133	80	16.6	4.82
AP	200	65	27.6	2.36
V_T—jet	52.5	30	6.276	4.78
V_T—plume	52.5	30	6.672	4.5
VK	50	44	6	7.33

Table S2. Calculation of τ_{mix} in the laboratory measurements of ref. 2 for the same conditions as in Fig. 4 in the main text

$(z - z_b)/L$	b (m)	u (m/s)	l (m)	l_E (m)	τ_{mix} (s)
0	0.025	0.0108	0.025	0.0125	1.5
1.15	0.036	0.0086	0.018	0.0036	0.7